

# IFSAR Processing for 3D Target Reconstruction

Christian D. Austin and Randolph L. Moses

The Ohio State University  
Department of Electrical and Computer Engineering  
2015 Neil Avenue, Columbus, OH 43210

## ABSTRACT

In this paper we investigate the use of interferometric synthetic aperture radar (IFSAR) processing for the 3D reconstruction of radar targets. A major source of reconstruction error is induced by multiple scattering responses in a resolution cell, giving rise to height errors. We present a model for multiple scattering centers and analyze the errors that result using traditional IFSAR height estimation. We present a simple geometric model that characterizes the height error and suggests tests for detecting or reducing this error. We consider the use of image magnitude difference as a test statistic to detect multiple scattering responses in a resolution cell, and we analyze the resulting height error reduction and hypothesis test performance using this statistic. Finally, we consider phase linearity test statistics when three or more IFSAR images are available. Examples using synthetic Xpatch backhoe imagery are presented.

**Keywords:** synthetic aperture radar, wide angle, radar imaging, interferometric SAR, three-dimensional reconstruction

## 1. INTRODUCTION

In this paper we investigate the use of interferometric synthetic aperture radar (IFSAR) processing for the 3D reconstruction of radar targets. In particular, we are interested in using two or more phase-coherent, high resolution SAR images taken at slightly offset elevation angles. The idea is to use phase difference from corresponding pixels in the image to estimate the height of scattering responses, where height is measured in the direction normal to the slant plane on which the images are formed.

Traditional IFSAR processing assumes that a given image pixel is dominated by scattering from a single height.<sup>1</sup> This height is then estimated from the phase difference between corresponding pixels in two images. In practice, the height estimate is corrupted by noise or clutter in the image; in some applications, height estimates can be locally averaged to reduce effects of the noise.<sup>1</sup>

The IFSAR application we consider is reconstruction of targets. For this application, it is expected that a major source of error may arise from scattering at more than one height in a given image resolution cell. This scattering can arise from layover (e.g. from tree canopies or other parts of the target) and also from multiple-bounce scattering mechanisms or sidelobes from strong scattering components in other resolution cells that leak into the image pixels under study. In this paper we analyze the effects of the presence of more than one scattering response on the resulting height estimate.

The approach we take is summarized as follows. We assume a model in which the IFSAR image pixels under study are the result of two scattering responses. Without loss of generality, we assume that there is a dominant scattering term at one height and a second, weaker term at a different height. We analyze the effect of this second term on IFSAR height estimates, as a function of scattering magnitude, its phase difference from the dominant scatterer, and its height difference from the dominant scatterer.

Second, we consider ways of detecting IFSAR pixels that are the result of more than one scattering center. We specifically consider the magnitude difference between IFSAR image pixels. We develop a statistical model for the joint probability of height errors and pixel magnitude errors, and develop a hypothesis test for detecting cells with more than one scattering center. We derive the RMS height error and the detection/false alarm probabilities for this hypothesis test. The analysis is aided by a geometric model that describes the tests, from which a qualitative detection and false alarm understanding can be derived. The test is applied to 3D object reconstruction from Xpatch SAR imagery of a backhoe ground target.

The notion of multiple scattering centers in a resolution cell fits into the framework of the general radar concept of unresolved targets, where each scattering center is a point-target. The problem is to estimate the location of the unresolved targets or to eliminate them from a radar image, if they detract from the image quality. This problem has been investigated in monopulse radar literature; a deterministic<sup>2</sup> solution and probabilistic<sup>3,4</sup> estimates of the location of two unresolved targets using monopulse radar system measurements have been developed. Here we model the problem of multiple unresolved scatterers from a SAR standpoint and investigate ways of improving 3D IFSAR images based on analysis of the model.

We also use the scattering model and geometric interpretation to predict performance when three or more coherent IFSAR images are available. We consider hypothesis tests for detecting multiple scattering centers, which are based on phase linearity of pixels under consideration. The analysis suggests that rejection of multiple-scattering cells is not significantly better using three or more IFSAR images than using only two images.

## 2. MULTIPLE SCATTERER MODEL

In this section we develop a model for two or more IFSAR images. We consider the case in which an image pixel is the result of a single dominant scattering center in a corresponding resolution cell. We also consider a model for the case when multiple scattering terms are present. The two-scattering model will be developed, although an extension to three or more scattering terms follows similarly.

### 2.1. Coherent IFSAR Images

We assume that a set of  $F$  complex images of a scene is available. Each image is formed from a SAR aperture at center elevation  $\Psi_i$  ( $i = 1, \dots, F$ ), and the images are formed on a common slant plane whose elevation is  $\Psi_s$ . We denote these images as  $s_i(x, y)$  for  $i = 1, \dots, F$ , where the  $x$ -axis and  $y$ -axis are oriented in the crossrange and downrange directions on the slant plane, respectively. For simplicity of exposition, we further assume that the data collection apertures are equally-spaced in elevation,

$$\Psi_i = \Psi_1 + (i - 1)\Delta\Psi, \quad i = 1, \dots, F \quad \text{and} \quad \Delta\Psi \ll 1 \quad (1)$$

where  $\Delta\Psi$  is a constant such that  $|\Psi_F - \Psi_1| \ll 1$ , and also that  $|\Psi_i - \Psi_s| \ll 1$ , so that  $\sin(\Psi_i - \Psi_s) \approx \Psi_i - \Psi_s$  and  $\cos(\Psi_i - \Psi_s) \approx 1$ .

In traditional IFSAR processing it is assumed that at each  $(x, y)$  location in the slant plane, backscatter occurs at a (single) height  $h(x, y)$  normal to the slant plane. In this case, for  $\Psi_i$  satisfying (1), the image pixel response  $s_i(x, y)$  at image location  $(x, y)$  is given by<sup>1</sup>

$$s_i(x, y) \approx \text{sinc}_{\Delta X, \Delta Y}(x, y) \otimes \left[ r(x, y) e^{-j4\pi \sin(\Psi_i - \Psi_s)h(x, y)/\lambda} e^{-j4\pi \cos(\Psi_i - \Psi_s)y/\lambda} \right] \quad (2)$$

$$\text{sinc}_{\Delta X, \Delta Y}(x, y) = \Delta X \Delta Y \text{sinc}\left(\frac{x\Delta X}{2\pi}\right) \text{sinc}\left(\frac{y\Delta Y}{2\pi}\right)$$

where  $\lambda$  is the (center frequency) wavelength of the radar and  $\Delta X$  and  $\Delta Y$  are the width of the support of the data collection in the crossrange and downrange Fourier dimensions  $X$  and  $Y$ . Here,  $r(x, y)$  is the reflectivity function of the scene, and  $h(x, y)$  is the height of the image above the slant plane. In a SAR system, the image in (2) is sampled, and the sample  $s_i(x_k, y_l)$  is denoted as the image pixel at  $(x_k, y_l)$ .

Traditional IFSAR processing forms an estimate of the height  $h(x, y)$  under the assumption that there is one scattering point per resolution cell. The  $z$ -coordinate of the image pixel can be calculated using the phase difference between two images at closely spaced elevation angles. The relation between image height and phase, for  $\Psi_i$  satisfying (1), is given by<sup>1</sup>

$$\gamma_i = \arg(s_{i+1}s_i^*) \approx k_I h(x, y). \quad (3)$$

where

$$k_I = \frac{4\pi\Delta\Psi}{\lambda} \quad (4)$$

is a proportionality constant that scales height to phase shift, and  $s_i$  is used to denote the image pixel value under consideration,  $s_i(x_k, y_l)$ , for simplicity of notation. From equation (3), the scattering height is estimated by

$$\hat{z}_i = \frac{1}{k_I} \arg(s_{i+1} s_i^*). \quad (5)$$

From equation (5) we see that IFSAR mapping from phase difference to height is ambiguous if the true phase difference exceeds  $2\pi$ . Hence, we define the unambiguous IFSAR height interval width as  $2\pi/k_I$ .

The resolution cell corresponding to an image pixel centered at some point  $(x_k, y_l)$  is given by

$$\mathbf{C}_{\mathbf{k},l} = \{(x, y, z) : x_k - \frac{x_{res}}{2} \leq x \leq x_k + \frac{x_{res}}{2}, y_l - \frac{y_{res}}{2} \leq y \leq y_l + \frac{y_{res}}{2}, \frac{-z_{max}}{2} \leq z \leq \frac{z_{max}}{2}\}, \quad (6)$$

where  $x_{res}$  and  $y_{res}$  are the resolutions in the x and y coordinates, respectively, and  $z_{max}$  is the maximum height range of the scene, which is often defined from the beamwidth of the radar. If more than one scatterer lies within cell  $C_{k,l}$ , equation (3) no longer applies. The image pixel corresponding to  $(x_k, y_l)$  is the combined response of the scatterers within that cell, and application of equation (3) may result in height estimation errors. We quantify these height errors in Section 3.

If the height of scattering varies slowly with respect to the SAR image resolution (such as in terrain-mapping applications), the single-pixel height estimate (5) can be modified to provide some averaging over multiple pixels.<sup>1</sup> However, in applications such as 3D target reconstruction, the scattering height varies rapidly with respect to image resolution, and height estimates are formed from single pixels to avoid bias due to smoothing. While much of the analysis that we present applies to the multiple-pixel case, we assume independent processing of individual pixels in the following.

In the ideal case of no noise and a single scattering response per pixel,  $\hat{z}_i = z_i$ . In practice, this height estimate will be corrupted by additional scattering terms and by noise. The effect of noise has been well-studied in the literature.<sup>1</sup> If each  $s_i$  measurement is corrupted by additive (complex) Gaussian noise with zero mean and variance  $\sigma_n^2$ , then for moderate to high SNR the height error is approximately Gaussian with zero mean and standard deviation given by

$$\text{stdev}(\hat{z}_i) = \frac{1}{k_I} \frac{\sigma_n}{|s_i|}. \quad (7)$$

The value of  $\sigma_n$  can be computed from knowledge of the SAR measurement system.<sup>1</sup> Another source of height error results when an image pixel is the superposition of more than one scattering response. These additional scattering responses could be effects of layover or multiple-bounce scattering whose responses project to the same image pixel. In the following sections, we will analyze the estimation error in the height estimate  $\hat{z}_i$  of the “desired” scattering center, that results from a nonzero extraneous scattering term. This error can be compared with the noise-induced error in equation (7) to determine when errors due to extraneous scattering are significant compared to errors due to noise.

## 2.2. Model Description

In the discussion that follows, a two-scatterer model is established. This model can be generalized to more than two scatterers, but the generalization is not needed here.

We assume that a set of  $F$  complex images of a scene are available. Consider an arbitrary image resolution cell, or pixel, centered at coordinates  $(x_k, y_l)$  in the image plane and let  $s_i$ ,  $i = 1, \dots, F$  denote the complex-valued pixel from the  $i$ th image. We assume that the scattering response that produces these values is comprised of two point scattering centers. The complex responses from the two scattering centers at elevation  $\Psi_1$  are given by  $A_1 e^{j\alpha_1}$  and  $A_2 e^{j\alpha_2}$ , respectively. Without loss of generality the first scattering center will be considered the dominant one,  $A_1 \geq A_2$ . We assume that the amplitude responses of the scattering centers are constant with respect to small elevation changes; however, the phase response is a function of elevation. These assumptions

follow from the arguments presented during the the development of equation (3) for one scatterer.<sup>1</sup> The two scatterer model is the superposition of each scatterer in the resolution cell. Thus, we have

$$s_i = A_1 e^{j\alpha_1} e^{j(i-1)k_I z_1} + A_2 e^{j\alpha_2} e^{j(i-1)k_I z_2}, \quad i = 1, \dots, F \quad (8)$$

$$\triangleq s_{i,1} + s_{i,2}$$

where  $z_1, z_2$  are the heights of the scattering centers (in meters) from the slant plane, and  $k_I$  is given by (4);  $s_{i,n}$  denotes the image pixel formed by the  $n^{th}$  scatter at elevation  $\Psi_i$ . A diagram of this model is shown in Figure 1(a).

### 2.3. Error Model

The height estimation due to multiple scattering terms is a function of six parameters, namely the scatterer amplitudes  $A_1$  and  $A_2$ , their response phases  $\alpha_1$  and  $\alpha_2$ , and their heights  $z_1$  and  $z_2$ . In this section, we develop an error model that reduces these six parameters to three parameters of interest, and we develop an intuitive geometric model that captures the essential characteristics of extraneous scattering on height estimation.

A vector diagram for  $s_i$  and  $s_{i+1}$  is shown in Figure 1(a). Using equation (5), the height estimate is given by the angle from  $s_i$  to  $s_{i+1}$ ,  $\phi_i$ , divided by a constant  $k_I$ .

To analyze the error resulting from two (or more) measurements containing two scattering terms, we consider the following error vector model. We define

$$\tilde{s}_i = \frac{s_i}{s_{i,1}} = 1 + \frac{A_2}{A_1} e^{j(\alpha_2 - \alpha_1)} e^{j(i-1)k_I(z_2 - z_1)} \quad i = 1, \dots, F \quad (9)$$

$$\triangleq 1 + f e^{j\alpha} e^{j\beta(i-1)} \quad (10)$$

The error model reduces the original six-parameter problem to one of three parameters. These three parameters of the error model have intuitive meanings. The parameter  $f = A_2/A_1$  ( $0 \leq f \leq 1$ ), represents the fractional magnitude of the second scatterer with respect to the first. The parameter  $\alpha$  is the difference in scattering response phases. The parameter  $\beta$  is an angle such that  $\beta/k_I$  is the height difference between the two scatterers. A vector diagram depicting these error terms is shown in Figure 1(b).

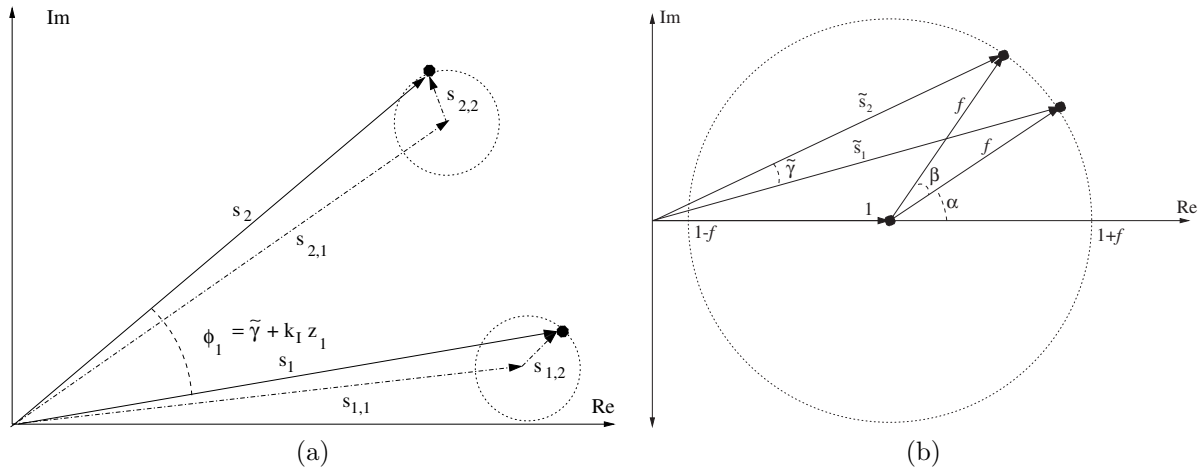


**Figure 1.** Vector diagrams for two point scattering model: (a) Unnormalized model (b) Normalized error model.

The angles between the  $s_i$  vectors encode a height estimate through the scaling factor  $k_I$ ; similarly, we define error angles as

$$\tilde{\gamma}_i = \arg(\tilde{s}_{i+1} \tilde{s}_i^*) \quad (11)$$

These angles encode the height errors given by

$$\tilde{z}_i = \hat{z}_i - z_{i,1} = \frac{1}{k_I} [\arg(s_{i+1}s_i^*) - \arg(s_{i+1,1}s_{i,1}^*)] = \frac{1}{k_I} [\arg(\tilde{s}_{i+1}\tilde{s}_i^*)] = \frac{1}{k_I} \tilde{\gamma}_i \quad (12)$$

derived from (5) and (9), using pixels in images at elevations  $\Psi_i$  and  $\Psi_{i+1}$ .  $\hat{z}_i$  is the estimated height of the image resulting from two scattering centers, and  $z_{i,1}$  is the height of the dominant scattering center; so, height error is the height that the estimate differs from the height of the dominant scatterer.

The error vector model in equation (10), and the corresponding angle errors in (11), provide a compact and geometric representation of the sources of height errors caused by a second scattering center. The parameters of  $\tilde{s}_i$  determine the height error, as we discuss in Section 3 for IFSAR height estimation when  $F = 2$  images are available. In Section 4 we address height estimation methods when  $F \geq 3$  coherent images are available, and discuss error mechanisms there.

### 3. IFSAR HEIGHT ANALYSIS USING TWO SAR IMAGES

Multiple scatterers in a resolution cell introduce height error into standard IFSAR processing. In this section we analyze errors obtained from height estimates found from two coherent SAR images (i.e.  $F = 2$  in (8)). We consider height estimation error resulting from the estimator in equation (5), and the utility of using scattering magnitudes to detect height errors; we hypothesize a detection statistic and analyze its performance. Our analysis assumes noiseless measurements of one or two scattering centers.

Standard IFSAR processing estimates the height from the angle difference between the two complex pixel values from two SAR images that are closely-spaced in elevation. The height error due to the presence of a second scattering term in the measurements is given by (12). Thus,  $\tilde{\gamma}$  characterizes height estimation error to within a constant  $k_I$ . We will analyze  $\tilde{\gamma}$  in the following discussion. We note a related application in which a similar scattering model arises is that of monopulse radar.<sup>2</sup> However, the statistical performance analysis and the generalization to three or more measurements presented in this paper appear to be novel, and in fact apply to the monopulse radar application as well.

Note that when  $A_2 = 0$ ,  $|s_1| = |s_2|$ , but when  $A_2 > 0$ ,  $|s_1|$  and  $|s_2|$  are in general not equal. This suggests a means of detecting the presence of a second scattering term. To this end, consider the normalized magnitude error

$$\tilde{m} = \frac{|s_1| - |s_2|}{|s_1| + |s_2|} = \frac{|\tilde{s}_1| - |\tilde{s}_2|}{|\tilde{s}_1| + |\tilde{s}_2|}. \quad (13)$$

The geometry in Figure 1(b) provides an intuitive understanding of both the angle and magnitude error. The error depends on  $f$ ,  $\alpha$ , and  $\beta$ . When either  $f = 0$  (i.e.  $A_2 = 0$ ) or  $\beta = 0$  (i.e.  $z_1 = z_2$ ), there is no angle or magnitude error, regardless of  $\alpha$ . Otherwise, both the error angle and magnitude depend on  $\alpha$ . Figure 2 shows four pairs of  $(\tilde{s}_1, \tilde{s}_2)$  that result in zero height or zero magnitude error, for fixed  $f$ , and  $\beta$ ; note that they are complimentary in the sense that  $\tilde{\gamma}$  achieves a local extremum when  $\tilde{m} = 0$ ; similarly, when  $\tilde{\gamma} = 0$ ,  $\tilde{m}$  is close to its maximum or minimum value.

Figure 3 shows the relationship between error angle,  $\tilde{\gamma}$ , and normalized magnitude error,  $\tilde{m}$ , for selected values of  $f$  and  $\beta$ , over all values of  $\alpha \in [0, 2\pi]$ . The minima and maxima relationship between  $\tilde{m}$  and  $\tilde{\gamma}$  discussed above can be seen in this figure. In addition, for fixed  $f$  ( $\beta$ ), smaller values of  $|\beta|$  ( $f$ ) result in smaller values for  $|\tilde{\gamma}|$  and  $|\tilde{m}|$ ; this can be seen from Figure 1(b). The complimentary nature of the extrema and zeros of  $\tilde{\gamma}$  and  $\tilde{m}$  are also evident.

#### 3.1. Probabilistic Model for IFSAR Height Error

The previous subsections characterize IFSAR height error for particular parameters  $f$ ,  $\alpha$ , and  $\beta$ . In order to better characterize overall height error performance, we propose a probabilistic model, in which we assume prior probabilities on these parameters and characterize the resulting probability density function (pdf) of the height error.

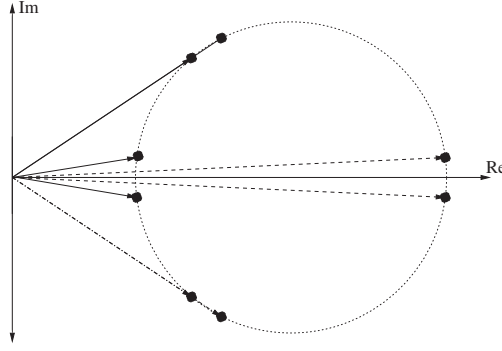


**Figure 2.** Vector diagram of four pairs of scattering vectors, corresponding to four values of  $\alpha$ , and illustrating how error magnitude difference  $\tilde{m}$  and error angle  $\tilde{\gamma}$  are complementary. Extremal values of  $\tilde{\gamma}$  are attained when  $\tilde{m} = 0$  (left and right pairs), and when  $\tilde{\gamma} = 0$  (top and bottom pairs) the normalized magnitude error is near its extremal values.

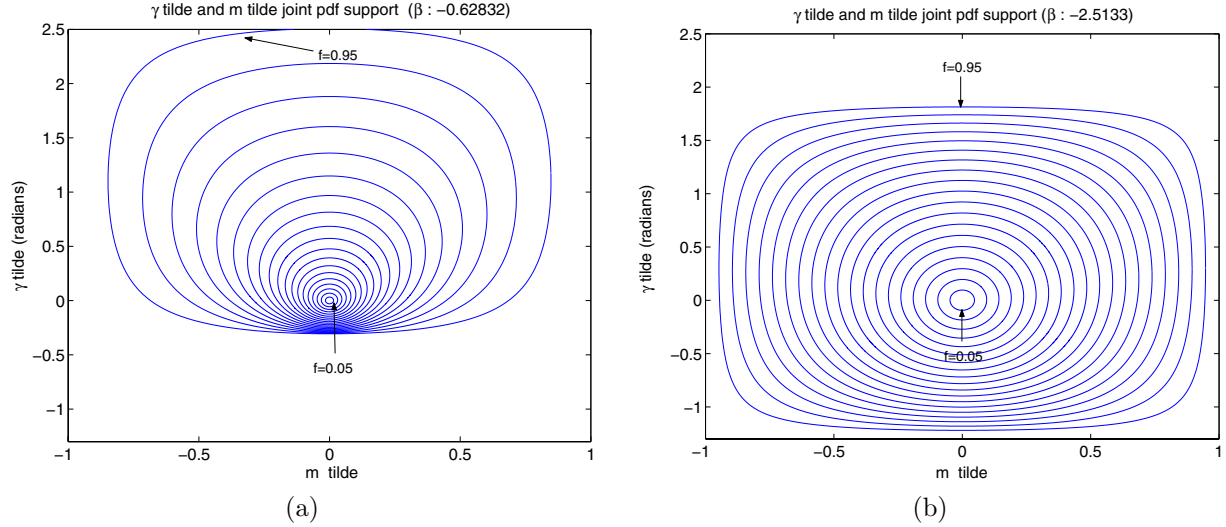


**Figure 3.** Plots of error angle  $\tilde{\gamma}$  and normalized magnitude error  $\tilde{m}$  for (a)  $\beta = -0.2\pi$  and (b)  $\beta = -0.8\pi$ . Each figure shows results for values of  $f \in [0, 0.95]$  at 0.05 increments and for all  $\alpha \in [0, 2\pi]$ .

Prior probabilities of the error parameters will depend on the application of interest, and in particular on the probabilistic characteristics of the physical parameters in the scene. We propose an example probabilistic model that applies to high-frequency (e.g. X-band) imaging of ground targets; other applications may dictate different priors.

Since knowledge of scattering response angle is often unknown or is highly sensitive to small changes in radar operating parameters, we assume that the relative phase  $\alpha$  of the backscattered response between the two scattering centers is uniformly distributed between  $-\pi$  and  $\pi$  (denoted  $\mathcal{U}(-\pi, \pi)$ ) throughout our analysis.

The conditional pdf of  $\tilde{\gamma}$  conditioned on  $\beta$  and  $f$ ,  $f_{\tilde{\gamma}|\beta,f}$ , can be derived analytically using the model in (10), but is omitted for brevity. Figure 4 shows two examples of  $f_{\tilde{\gamma}|\beta,f}$  for two sets of  $\beta$  and  $f$ . The pdfs have significant peaks at around the minimum and maximum values of  $\tilde{\gamma}$ , and most of the probability is concentrated around these values. The general shape of the conditional pdf can also be predicted from the vector diagram in Figure 1(b); varying  $\alpha$  corresponds to traversing around the circle, and for most values of  $\alpha$ ,  $\gamma$  will be non-zero;

this implies that most of the density will be located away from zero. Further analysis will show that most error angles are in fact close to the minimum and maximum error angles.

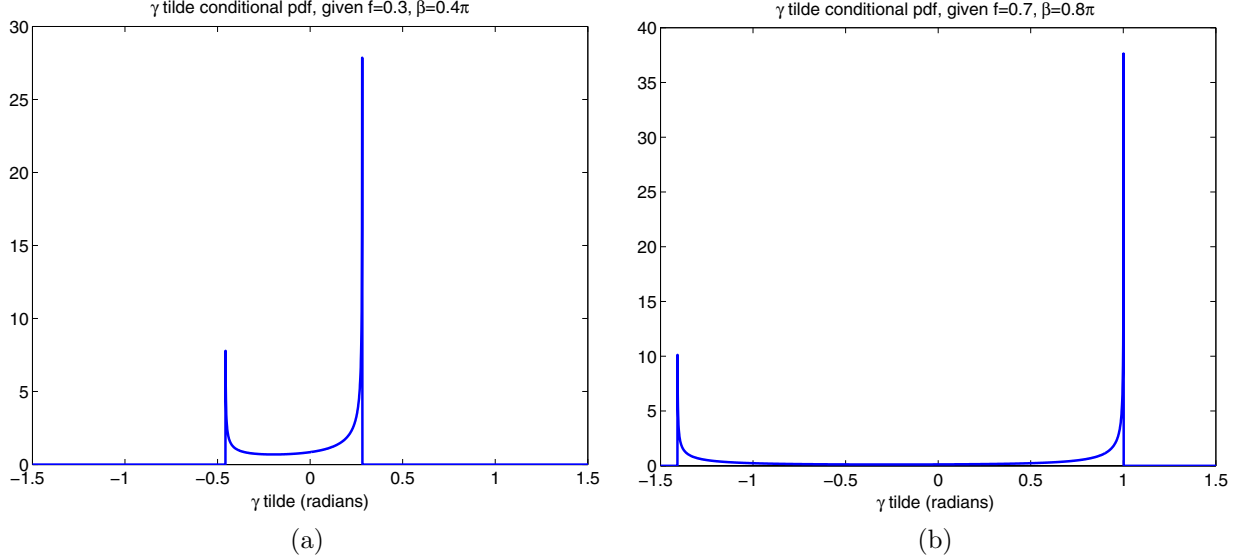


**Figure 4.** Conditional pdf of  $\tilde{\gamma}$  given  $f$  and  $\beta$ , for (a)  $f = 0.3$  and  $\beta = 0.4\pi$ ; (b)  $f = 0.7$  and  $\beta = 0.8\pi$ .

The conditional pdf,  $f_{\tilde{\gamma}|\beta,f}$ , can be used to find the unconditional pdf of gamma,  $f_{\tilde{\gamma}}$ , by integrating out the priors.  $f_{\tilde{\gamma}}$  summarizes the error introduced by an additional scattering center in a resolution cell. Thus, to find the unconditional density, we need to define a prior pdf for  $\beta$  and for  $f$ . Recalling that  $\beta$  relates to the physical height difference of interfering scattering terms, its distribution describes the difference between the height of a desired scattering center and that of an interfering one. We will assume a uniform pdf  $\beta \sim \mathcal{U}[-\pi, \pi]$ , to model cases in which layover (say, from trees) may occur at any height. A truncated Gaussian pdf  $\beta \sim \mathcal{TN}_{[-\pi, \pi]}(0, \sigma_\beta^2)$ , where  $\mathcal{TN}_{\text{support}}(\mu, \sigma)$  is a normal distribution with mean  $\mu$  and standard deviation  $\sigma$  truncated to finite support and renormalized, will also be considered. This latter model might describe interfering scattering from other points on the target of interest, in which case the height of the interfering scatterer is likely to be limited by the height of the target (measured from the SAR slant plane). We assume no knowledge of  $f$ , except its maximum value. This parameter will be modeled as a uniform prior,  $f \sim \mathcal{U}[0, f_{\max}]$ . Using these prior pdfs, we present results that predict height estimation error performance for cases of interest.

Figure 5 shows examples of the conditional pdf of  $\tilde{\gamma}$  given a fixed value of  $f$ ,  $f_{\tilde{\gamma}|f}$ , for the two choices for the prior on  $\beta$  discussed above. These pdfs are found from the conditional pdfs,  $f_{\tilde{\gamma}|\beta,f}$  by integrating out  $\beta$ . The truncated normal pdf in Figure 5(b) is chosen such that the standard deviation of the height difference between the desired and interfering scattering center is 1 meter for a typical X-band radar scenario ( $\lambda = 0.029$  m,  $\Delta\Psi = 0.05^\circ$ ), where the elevation angles satisfy (1); for this parameter selection  $k_I = 0.373$  rad/m; so, 1 radian in Figure 5 corresponds to a height error of 2.68m.

We see that error angle probability in Figure 5 is concentrated about zero, instead of the tails of the distribution support, as was the case for fixed  $f$  and  $\beta$ . This behavior is exhibited over all  $f$ , and hence, assuming  $f$  to be a uniform prior,  $f_{\tilde{\gamma}}$  will have the same general shape, as shown in Figure 8.

The maximum and RMS errors of  $\tilde{\gamma}$  are summarized in Figure 6. Figure 6(a) displays the RMS error angle with  $f \sim \mathcal{U}[0, f_{\max}]$  for priors on  $\beta$  chosen to be uniform and truncated normal; Figure 6(b) compares the maximum error to the RMS error angle for uniform  $\beta$  and a given interfering scattering center relative magnitude,  $f$ . This figure demonstrates how error angle is affected by the relative magnitude of the interfering scattering center. As might be expected, RMS error for the case when the interfering scattering height can be anywhere is larger than when the interfering scattering height is close to the dominant scattering center height with high probability, and RMS error is monotonic increasing as a function of the relative magnitude of the interfering scattering center.

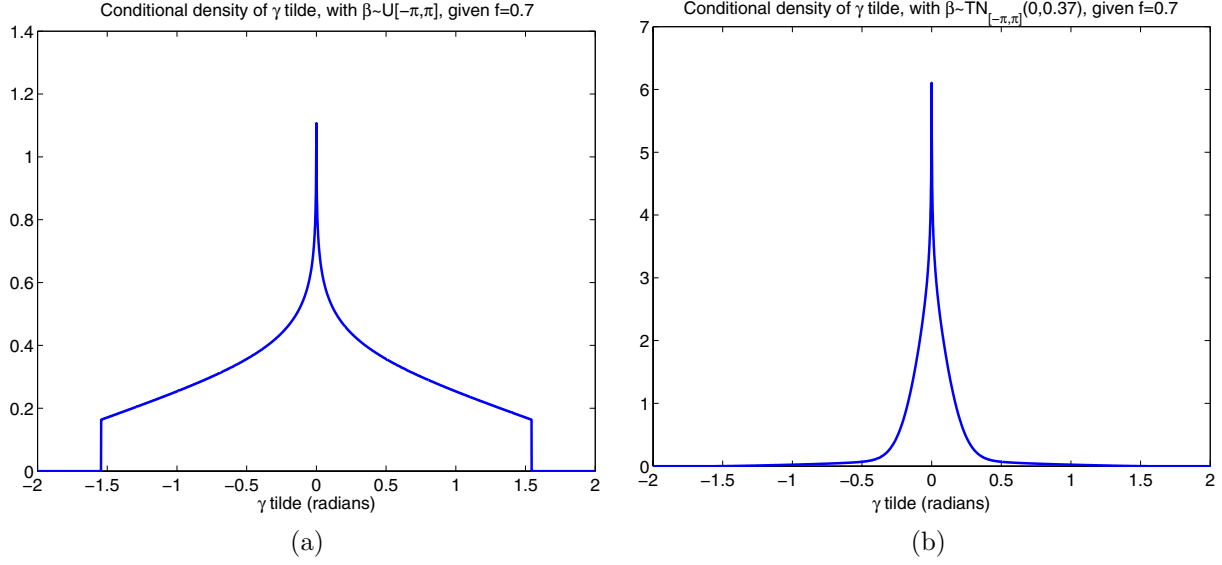


**Figure 5.** Conditional pdf of  $\tilde{\gamma}$  for fixed  $f = 0.7$  and two choices for the prior pdf of  $\beta$ . (a)  $\beta \sim \mathcal{U}[-\pi, \pi]$ . (b)  $\beta \sim \mathcal{TN}_{[-\pi, \pi]}(0, 0.37)$ .

Figure 6 provides a mechanism for analyzing IFSAR height error as a function of prior distributions on the parameters in (10). For example, we see from Figure 6(b) that, under these assumed prior probabilities on  $\beta$  and X-Band radar parameters, the RMS height estimation error,  $\frac{1}{k_I} \sigma_{\tilde{\gamma}}$ , is less than 1 meter if  $f_{max} < 0.36$ .

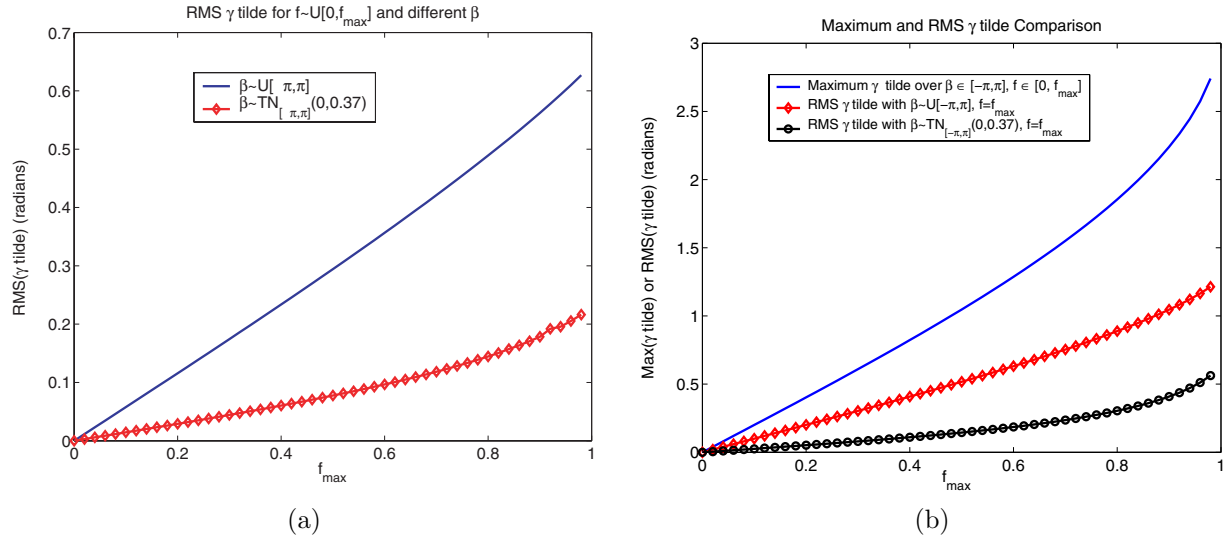


**Figure 6.** (a) RMS error angle for priors  $f \in \mathcal{U}[0, f_{max}]$ ,  $\beta \sim \mathcal{U}[-\pi, \pi]$ , and  $\beta \sim \mathcal{TN}_{[-\pi, \pi]}(0, 0.37)$ , (b) Maximum error angle, RMS error angle for fixed  $f = f_{max}$  and  $\beta \sim \mathcal{U}[-\pi, \pi]$ , and RMS error angle for fixed  $f = f_{max}$  and  $\beta \sim \mathcal{TN}_{[-\pi, \pi]}(0, 0.37)$ .

The preceding analysis complements a traditional noise error analysis for standard IFSAR. In particular, we can compare RMS height errors resulting from interference to those resulting from noise as given in equation (7).



### 3.2. Height Error Detection from Pixel Magnitudes

In this section we consider a method of detecting instances of large height error by using the pixel magnitudes corresponding to the two coherent SAR images. In particular, we analyze the efficacy of the  $\tilde{m}$  feature in identifying pixels for which the height estimation error is high. Intuitively, the argument goes as follows. If  $A_2 = 0$  (i.e., there is no interference scattering present), then  $|s_i|$  are equal for  $i = 1, \dots, F$ , and  $\tilde{s}_i \equiv 1$ . Thus, one might consider testing the (relative) magnitude difference between  $\tilde{s}_1$  and  $\tilde{s}_2$  as a way of detecting interference, and thus detecting height errors.

A detection test using  $\tilde{m}$  would keep height estimates if the relative pixel magnitudes are (nearly) equal, and reject height estimates otherwise; that is, the decision rule is

$$\begin{cases} \text{if } |\tilde{m}| \leq \eta_m, & \text{keep height estimate} \\ \text{if } |\tilde{m}| > \eta_m, & \text{reject height estimate} \end{cases} \quad (14)$$

where  $\eta_m$  is some prescribed threshold. If the test is effective, height error will be small for accepted height estimates and large for the rejected estimates; that is,  $\tilde{\gamma}$  is small when  $\tilde{m}$  is small (recall that  $\tilde{\gamma}$  is proportionally to the height estimation error).

We first consider this detection approach from a geometric perspective, using the vector signal diagram in figure 1(b) or figure 2. Consider fixed values of  $f$  and  $\beta$ . We see that the signal magnitudes  $|\tilde{s}_1|$  and  $|\tilde{s}_2|$  are nearly equal,  $\tilde{m} \approx 0$ , for values of  $\alpha$  near 0 and  $\pi$ ; that is, when the two points are near the leftmost or rightmost parts of the dotted circle. For these regions, however,  $\tilde{\gamma}$  achieves its extremal values, so the height estimate error is maximum. Thus, for fixed  $f$  and  $\beta$ , the proposed detection procedure does the opposite of what we desire. However, our approach considers  $f$  and  $\beta$  over intervals of values; the performance of the test in this case is discussed next.

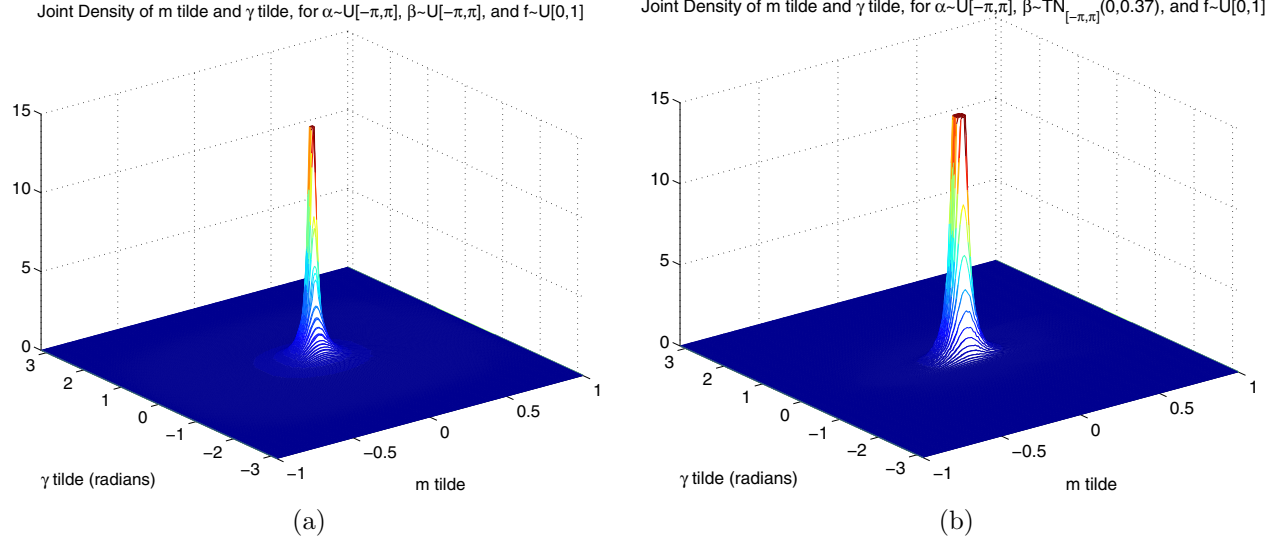
Observing how  $f$  and  $\beta$  vary in Figure 3 also provides geometric insight. The test  $|\tilde{m}| \leq \eta_m$  corresponds to accepting all points in a vertical “ribbon” centered at  $\tilde{m} = 0$  in these figures. An ideal test would be to accept all points for which  $|\tilde{\gamma}| < \eta_{\tilde{\gamma}}$ , which is a horizontally-oriented “ribbon”, but  $\tilde{\gamma}$  cannot be measured; so, a test cannot be applied to it directly. For small values of  $f$ , when  $|\tilde{m}| \leq \eta_m$ ,  $\tilde{\gamma}$  will also be small. However, for larger values of  $f$ ,  $\tilde{\gamma}$  may be very large even for small values of  $\tilde{m}$ . We investigate this observation and determine if  $\eta_m$  can be set so that the probability of large error angle pixels will decrease when the threshold is applied.

The above insights can be made more quantitative by considering the joint pdf of  $\tilde{m}$  and  $\tilde{\gamma}$ ,  $f_{\tilde{\gamma}, \tilde{m}}$ . Figure 7 shows two versions of  $f_{\tilde{\gamma}, \tilde{m}}$  calculated for two choices of prior distributions on  $f$  and  $\beta$ .

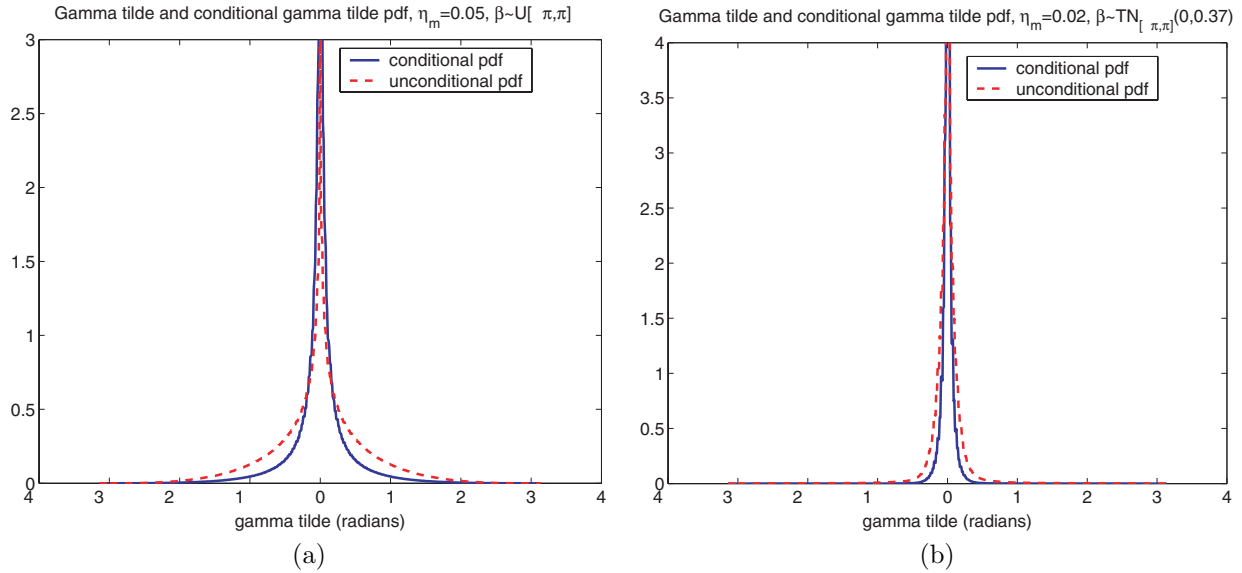
A noteworthy feature of these pdfs is that most of their density is concentrated about a region centered at  $(\tilde{m}, \tilde{\gamma}) = (0, 0)$ . This suggests that the threshold filter introduced in (14) will not be able to reject all pixels with large error angle, but a majority of the accepted pixels will have error angles close to zero.

Figure 8 shows conditional pdfs of  $\tilde{\gamma}$  overlaid on unconditional pdfs of  $\tilde{\gamma}$ . All are derived from the distributions in Figure 7 and the conditional pdfs in Figures 8(a) and (b) are conditioned on the events  $\{\eta_m = 0.05\}$ , and  $\{\eta_m = 0.02\}$ , respectively. In both cases, the conditional pdfs have more probability concentrated at low error angles than the unconditional pdfs do. So, the probability that error angle is below a certain level will be higher for the conditioned than for the unconditioned case. We note that approximately 70% of pixels are rejected using  $\eta_m = 0.05$  in the  $\beta \sim \mathcal{U}[-\pi, \pi]$  case, and about 53% are rejected in the  $\eta_m = 0.02$  and  $\beta \sim \mathcal{TN}_{[-\pi, \pi]}(0, 0.37)$  case.

As suggested by Figure 8, threshold filtering does improve RMS error performance, as compared to the unfiltered case; furthermore, the value of a threshold and its effectiveness are a function of the distribution on  $\beta$ . These hypotheses are supported by the RMS plots shown in Figure 9 (a) and (b), which show the RMS error angle as a function of threshold values and the percentage of points rejected versus threshold for the two conditional pdfs in Figure 8. The RMS plots are monotonically increasing as a function of  $\eta_m$ , and  $\eta_m = 1$  corresponds to having no threshold. Recall that for the X-band radar system considered,  $k_I = 0.373$  rad/m, so RMS height errors with no thresholding are approximately 1.7 m for the distribution in Figure 8(a) and 0.64 m for the distribution in Figure 8(b). In both cases, a threshold of  $\eta_m \approx 0.05$  results in decreasing the RMS height error by one-half, and eliminates around 25% and 75% of the pixel pairs, respectively.



**Figure 7.** Joint pdf of  $\tilde{\gamma}$  and  $\tilde{m}$ ,  $f_{\tilde{\gamma}, \tilde{m}}$  when (a)  $f \sim \mathcal{U}[0, 1]$  and  $\beta \sim \mathcal{U}[-\pi, \pi]$ ; (b)  $f \sim \mathcal{U}[0, 1]$  and  $\beta \sim \mathcal{TN}_{[-\pi, \pi]}(0, 0.37)$ . Both pdfs peak at  $(0, 0)$ , but the figures are clipped near  $\tilde{\gamma} = \tilde{m} = 0$  to more clearly illustrate the pdf shapes.



**Figure 8.** Comparison of  $f_{\tilde{\gamma}}$  and  $f_{\tilde{\gamma}|\eta_m}$  for  $f \sim \mathcal{U}[0, 1]$  and (a)  $\beta \sim \mathcal{U}[-\pi, \pi]$  and  $\eta_m = 0.05$ , (b)  $\beta \sim \mathcal{TN}_{[-\pi, \pi]}(0, 0.37)$  and  $\eta_m = 0.02$

Figure 10 shows a ROC curve for a binary hypothesis testing problem, in which the hypotheses are:

$$\begin{aligned} H_0 &: \{|\tilde{\gamma}| \geq \eta_\gamma\} \\ H_1 &: \{|\tilde{\gamma}| < \eta_\gamma\} \end{aligned} \quad (15)$$

and (14) is the decision rule. The pdf used,  $f_{\tilde{\gamma}, \tilde{m}}$ , was derived from  $\beta \sim \mathcal{TN}_{[-\pi, \pi]}(0, 0.37)$  and  $f \sim \mathcal{U}[0, 1]$ . For the X-band radar considered previously,  $k_I = 0.373$  rad/m, so choosing  $\eta_\gamma = 0.1119$  results in testing for height

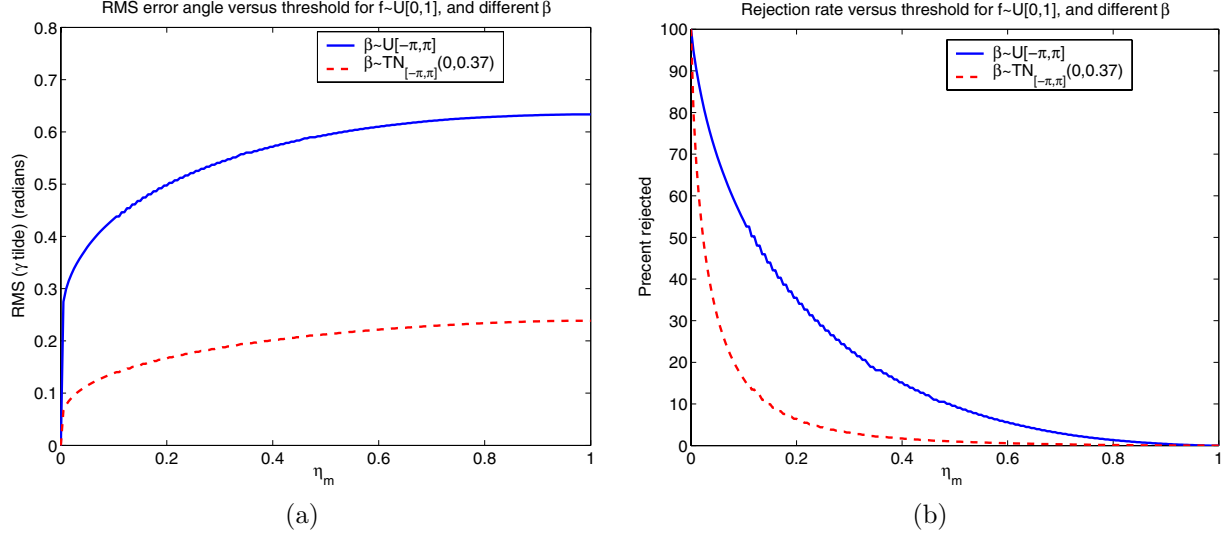


**Figure 9.** (a) Conditional RMS error of  $f_{\tilde{\gamma}|\eta_m}$  as a function of  $\eta_m$  (b) Image pixel rejection percentage.

errors less than 0.3 m, and  $\eta_\gamma = 0.1865$  tests for height errors less than 0.5 m.

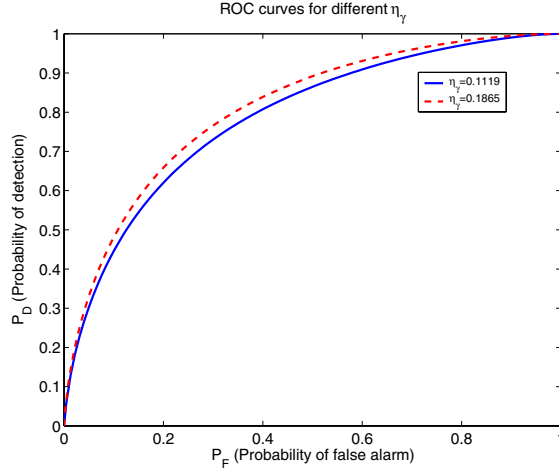


**Figure 10.** ROC curve showing probability of detection of the event  $\{|\tilde{\gamma}| \leq \eta_\gamma\}$  versus its probability of false alarm, using  $\tilde{m}$  as a test statistic for the pdf  $f_{\tilde{\gamma}, \tilde{m}}$  derived with  $\beta \sim \mathcal{TN}_{[-\pi, \pi]}(0, 0.37)$  and  $f \sim \mathcal{U}[0, 1]$ .

This analysis shows that thresholding on  $\tilde{m}$  does decrease the percentage of image pixels with large height error. The effectiveness of this threshold depends on the prior distribution of  $\beta$ ,  $\alpha$  and  $f$ . Given that 3D image quality is also a function of the number of pixels used in reconstruction, the rejection rate should also be considered when choosing a threshold.

#### 4. HEIGHT ERROR DETECTION FROM THREE OR MORE COHERENT IMAGES

The previous analysis considered the case in which two coherent SAR images were used to estimate scattering height. In this section we consider the use of three or more SAR images.

One advantage of multiple images is that one can compute phase differences  $\gamma_i$  between two or more image pairs. For the case of no interference scattering ( $A_2 = 0$ ), these phase differences are all equal. Thus, one might

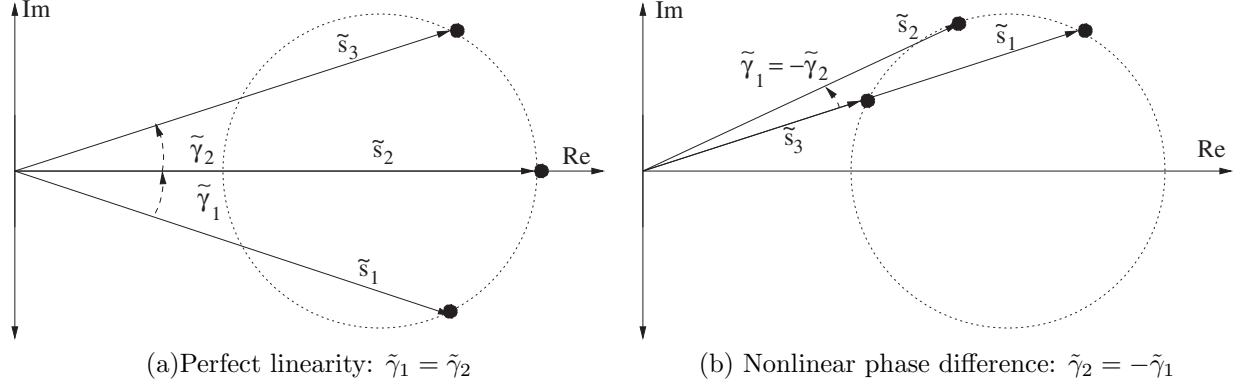


**Figure 11.** Vector diagram of resultant vectors at three elevation angles, (a) when the phases of  $\tilde{s}_1$ ,  $\tilde{s}_2$ , and  $\tilde{s}_3$  are perfectly linear; (b) when the phases are nonlinear.

consider a test for detecting interference, and, hence, detecting cases in which height estimation error is large, by testing whether the phase differences are equal, or, equivalently by testing whether the phases are linear. Such a test would involve testing whether  $|\gamma_2 - \gamma_1| = |\tilde{\gamma}_2 - \tilde{\gamma}_1| > \eta_\gamma$  for some prescribed threshold  $\eta_\gamma$ ; if so, the phase linearity hypothesis is rejected. More sophisticated tests could use a more general combination of the phases and magnitudes from these  $F$  pixel values.

We submit that such tests have at best minor improvements over the detection test using two SAR images that is described in the previous section. We provide a geometric argument based on the vector diagram in Figure 11.

In this figure, we show the error vector diagram for  $F = 3$ , giving two image pairs (the figure and argument is similar for  $F > 3$ ), and for two values of  $\alpha$ . When  $\alpha = -\beta$ , then  $\tilde{\gamma}_1 = \tilde{\gamma}_2$ , and the phase linearity hypothesis is accepted for any threshold value. However, the resulting height estimate is in error by the amount  $\frac{1}{k_I} \tilde{\gamma}_1$ . In the second case, we have  $\tilde{\gamma}_1 = -\tilde{\gamma}_2$ , so the phase is maximally nonlinear over all values of  $\alpha$ ; on the other hand, the best linear phase fit effectively averages the phase errors  $\tilde{\gamma}_1$  and  $\tilde{\gamma}_2$ , so the scattering height estimation error is zero in this case. Thus, phase linearity is complimentary to angle error  $\tilde{\gamma}$  in the same manner as magnitude error  $\tilde{m}$  is complimentary to angle error  $\tilde{\gamma}$  for the two-image case discussed in the previous section. We thus see that the phase linearity detection test fails to detect large height errors for precisely those cases in which the  $F = 2$  magnitude error test fails. As a result, the detection test using  $F = 3$  is not expected to have significantly better performance than the  $F = 2$  case. This reasoning applies also for  $F > 3$ . Given the additional (high) cost of collecting SAR data over several elevations, it does not appear that this cost is justified in terms of reducing scattering height errors caused by multiple scattering terms in a resolution cell.

The above arguments apply to interference scattering terms, and assume noiseless data. In practice, of course, the additional SAR images can be used to reduce the effects of height estimation error caused by noise. However, this reduction is modest; the height estimation standard deviation decreases at a rate of  $\sqrt{F}$ .

When  $F \geq 4$ , it is possible to simultaneously estimate the magnitudes and phases of both scattering terms in (8) using Prony's method.<sup>5</sup> There are some reasons to avoid a Prony-based approach, however. First, Prony's method is very sensitive to noise, and the height estimation error due to noise could exceed the estimation error due to bias from interfering scatterers in standard IFSAR processing. Second, Prony's method is sensitive to modeling errors, and (highly) biased height estimates could result if the scattering response is composed of three or more scattering centers, a case that could well happen in practice. For these reasons, Prony's method is not expected to provide reduced height errors for this problem.

## 5. EXAMPLE: BACKHOE IFSAR PROCESSING

In this section we present illustrative results of IFSAR processing to form a 3D reconstruction of a ground vehicle. Specifically, we consider a construction backhoe as shown in Figure 12(a). Using XpatchT scattering prediction

software and a CAD model of the backhoe, high resolution, fully-polarimetric SAR images are generated across the entire “upper hemisphere” above the vehicle. Pairs of SAR images at the same azimuth and separated by  $0.05^\circ$  in elevation are used for coherent IFSAR processing, and are denoted as IFSAR image pairs.

Figure 12 shows results in which 3D scattering center locations are estimated from IFSAR image pairs, and then overlaid on a common coordinate system. The image pairs are centered every  $5^\circ$  in azimuth from  $0^\circ$  to  $355^\circ$ , and at elevations of  $5n^\circ$  and  $(5n + 0.05)^\circ$  for  $n = 0, \dots, 17$ . Each SAR image has resolution of approximately  $2\text{in} \times 2\text{in}$ , and each is processed to extract pixels whose RCS is within 40dB of the global RCS peak value; the height of each scattering center is estimated by applying equation (5) to each image pair. Finally, pixels are mapped to a common coordinate system and plotted. In Figure 12(b), all points are plotted, whereas in Figure 12(c), only points that pass a magnitude error threshold test in (14) are plotted. The threshold,  $\eta_m$  in this case is chosen to be 0.01. Points eliminated by the threshold test are shown in Figure 12(d).

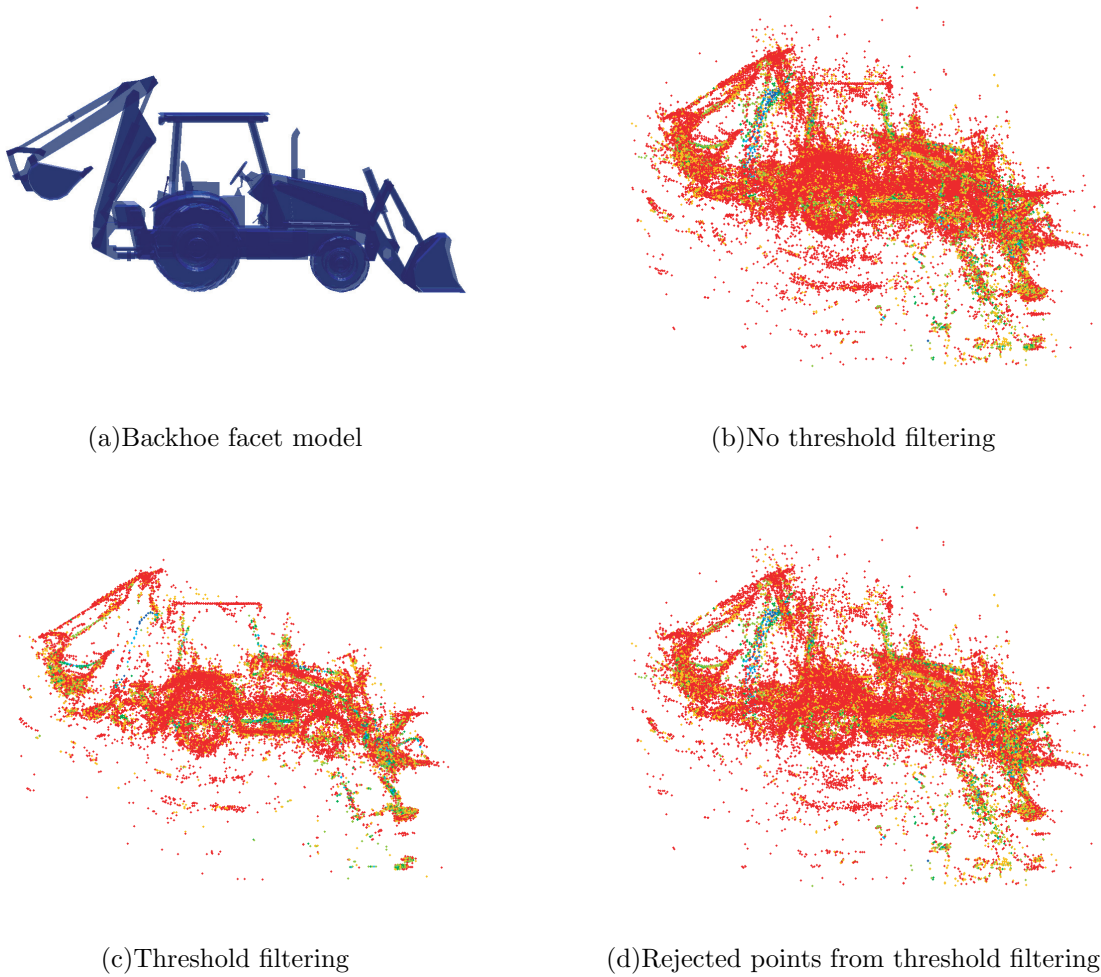


**Figure 12.** 3D IFSAR reconstruction of a backhoe from two IFSAR images, with and without threshold filtering. (a) Backhoe facet model (b) IFSAR image of all points 40 dB from the global RCS maximum (c) IFSAR image of all points 40 dB from the global RCS maximum and  $\tilde{m} \leq \eta_m = 0.01$  (d) IFSAR image of all points 40 dB from the global RCS maximum and  $\tilde{m} > \eta_m = 0.01$ . In (b),(c),and (d), larger points correspond to scattering centers with larger RCS values.

These figures illustrate the effect that thresholding  $\tilde{m}$  has on the 3D reconstruction of IFSAR data. In Figure 12 (b), the shape of the backhoe can be seen from the IFSAR generated points, but the image is surrounded by many points that do not appear to correspond to a part of the backhoe. Figure 12 (c), showing the image

after threshold filtering, is sharper than the image in (b), as many of the points not close to a backhoe surface are eliminated; these points are shown in Figure 12 (d). It should be noted that the threshold  $\eta_m$  was chosen qualitatively. If distributions on the priors  $f$ ,  $\beta$  for the backhoe were known, a more suitable threshold may be found using the analysis in section 3. It should also be mentioned that Figures (b) and (d) are zoomed in and contain points outside the region of view, which were not present in (c).

## 6. CONCLUSION

In this paper, we investigated IFSAR 3D image reconstruction when there is more than one scattering center per resolution cell. We developed a mathematical error model of two scattering centers per resolution cell. This model consists of three parameters, all with physical meaning with respect to the scattering centers in the resolution cell; furthermore, this model can be represented pictorially as a complex vector diagram. Using this model, a probabilistic description of height error (error angle  $\tilde{\gamma}$ ) and normalized image magnitude difference ( $\tilde{m}$ ) was presented. RMS height error was analyzed for different distributions on model parameters. RMS analysis allows for comparison with IFSAR error introduced by noise. A threshold test on the  $\tilde{m}$  statistic was introduced, and its effectiveness in reducing RMS height error was examined. This test did prove successful in reducing RMS height error, but its effectiveness depends on the distribution of the error model parameters. When setting a threshold, RMS height error and the percent of data rejected should be considered simultaneously because of the trade off in 3D image quality between the two. Testing for phase linearity using more than two elevation angles appears to offer little improvement in reducing error over the use of two elevation angles and a threshold on  $\tilde{m}$ , and for more than three elevation angles, Prony's method could be used to estimate the complex value of each scatter, but it is very sensitive to deviations from an ideal noiseless mathematical model. To conclude, the  $\tilde{m}$  threshold test was used to filter XpatchT backhoe data. The image with filtering appeared sharper than the one without filtering, showing that  $\tilde{m}$  threshold filtering is capable of improve 3D IFSAR image quality.

## REFERENCES

1. C. V. Jakowatz Jr., D. E. Wahl, P. H. Eichel, D. C. Ghiglia, and P. A. Thompson, *Spotlight-Mode Synthetic Aperature Radar: A Signal Processing Approach*, Kluwer Academic Publishers, Boston, 1996.
2. S. M. Sherman, *Monopulse Principles and Techniques*, Artech House, Dedham, MA, 1984.
3. W. Blair and M. Brandt-Pearce, "Monopulse doa estimation of two unresolved rayleigh targets," *IEEE Transactions on Aerospace and Electronic Systems* **37**, pp. 452–469, April 2001.
4. W. Zhen, A. Sinha, P. Willett, and Y. Bar-Shalom, "Angle estimation for two unresolved targets with monopulse radar," *IEEE Transactions on Aerospace and Electronic Systems* **40**, pp. 998–1019, July 2004.
5. S. M. Kay, *Modern Spectral Estimation, Theory and Application*, Prentice Hall, Englewood Cliffs, NJ, 1988.